

# The ionized X-ray outflowing torus in ESO 323–G77: low-ionization clumps confined by homogeneous warm absorbers

M. Sanfrutos,<sup>1★</sup> G. Miniutti,<sup>1</sup> Y. Krongold,<sup>2</sup> B. Agís-González<sup>1</sup>  
and A. L. Longinotti<sup>2,3,4</sup>

<sup>1</sup>Centro de Astrobiología (CSIC–INTA), Dep. de Astrofísica, ESAC, PO Box 78, Villanueva de la Cañada, E-28691 Madrid, Spain

<sup>2</sup>Instituto de Astronomía, Universidad Nacional Autónoma de México, Apdo. 70-264, Cd. Universitaria, México DF 04510, Mexico

<sup>3</sup>European Space Astronomy Centre of ESA, PO Box 78, Villanueva de la Cañada, E-28691 Madrid, Spain

<sup>4</sup>Catedrática CONACYT - Instituto Nacional de Astrofísica, Óptica y Electrónica, Luis E. Erro 1, Tonantzintla, Puebla, México, C.P. 72840

Accepted 2015 December 17. Received 2015 December 14; in original form 2015 May 8

## ABSTRACT

We report on the long- and short-term X-ray spectral analysis of the polar-scattered Seyfert 1.2 galaxy ESO 323–G77, observed in three epochs between 2006 and 2013 with *Chandra* and *XMM–Newton*. Four high-resolution *Chandra* observations give us a unique opportunity to study the properties of the absorbers in detail, as well as their short time-scale (days) variability. From the rich set of absorption features seen in the *Chandra* data, we identify two warm absorbers with column densities and ionizations that are consistent with being constant on both short and long time-scales, suggesting that those are the signatures of a rather homogeneous and extended outflow. A third absorber, ionized to a lesser degree, is also present and it replaces the strictly neutral absorber that is ubiquitously inferred from the X-ray analysis of obscured Compton-thin sources. This colder absorber appears to vary in column density on long time-scales, suggesting a non-homogeneous absorber. Moreover, its ionization responds to the nuclear luminosity variations on time-scales as short as a few days, indicating that the absorber is in photoionization equilibrium with the nuclear source on these time-scales. All components are consistent with being co-spatial and located between the inner and outer edges of the so-called dusty, clumpy torus. Assuming co-spatiality, the three phases also share the same pressure, suggesting that the warm / hot phases confine the colder, most likely clumpy, medium. We discuss further the properties of the outflow in comparison with the lower resolution *XMM–Newton* data.

**Key words:** galaxies: active – X-rays: galaxies.

## 1 INTRODUCTION

Active galactic nuclei (AGN) ordinarily show X-ray spectral variability on months to years time-scales, which is often related to absorption phenomena (e.g. Risaliti, Elvis & Nicastro 2002; Agís-González et al. 2014; Miniutti et al. 2014). In many cases, such long-term absorption variability can be associated with the transit of dusty clouds in our line of sight (LOS), which reveals the presence of a clumpy, dusty torus at relatively large spatial scales (see e.g. Agís-González et al. 2014; Markowitz et al. 2014).

In the last few years, various examples of absorption variability within time-scales as short as hours or days have been reported, such as in NGC 4388, NGC 4151, NGC 1365, NGC 7582, and SWIFT J2127.4+5654, as reported in Elvis et al. (2004), Puccetti et al. (2007), Risaliti et al. (2009b), Bianchi et al. (2009), and

Sanfrutos et al. (2013), respectively. As an example, the in-depth study of the short time-scale absorption variability in SWIFT J2127.4+5654 reveals unambiguously the transit of a single cloud in the LOS to a fairly compact X-ray source (few gravitational radii in size). Usually, the short time-scale absorption variability data are in good agreement with the existence of a set of dense, cold clouds with characteristic column densities of  $10^{23}$ – $10^{24}$  cm<sup>−2</sup>, physical densities of  $10^9$ – $10^{11}$  cm<sup>−3</sup>, and velocities of the order of  $10^3$  km s<sup>−1</sup> orbiting the X-ray source at radii of  $10^3$ – $10^4$   $r_g$ , where  $r_g = GM/c^2$  is the gravitational radius for a black hole of mass  $M$ . These properties suggest to identify the obscuring clouds with the same clouds that are responsible for the emission of broad optical/ultraviolet (UV) emission lines, i.e. with clouds in the broad line region (BLR).

In the following we report results from four high-resolution *Chandra* observations of ESO 323–G77 taken between 2010 April 14 and 24. ESO 323–G77 is a bright (13.56 mag) polar-scattered Seyfert 1.2 galaxy (Véron-Cetty & Véron 2006) at  $z = 0.015$

\* E-mail: sanfrutoscm@cab.inta-csic.es

(Dickens, Currie & Lucey 1986). It was first classified as an AGN by Fairall (1986). The symmetry axis inclination of ESO 323–G77 is most likely of  $\sim 45^\circ$  with respect to our LOS (Schmid, Appenzeller & Burch 2003), intermediate between the characteristic inclination of Seyfert 1 and Seyfert 2 galaxies. Our viewing angle is therefore likely grazing the edge of the obscuring matter, namely the torus of the unified model (Antonucci 1993). In order to perform a more complete analysis and to compare the absorbers’ properties at different epochs, data from two high-quality *XMM–Newton* observations are also included from 2006 February 7 (Jiménez-Bailón et al. 2008) and 2013 January 17 (Miniutti et al. 2014).

## 2 X-RAY OBSERVATIONS

*XMM–Newton* first observed ESO 323–G77 on 2006 February the 7 for a total net exposure time of  $\sim 23$  ks. Then, *Chandra* observed the source on four occasions in 2010 April with the High-Energy Transmission Grating Spectrometer (HETGS): on the 14th (ID: 11848, for a total net exposure time of  $\sim 46$  ks), on the 19th (ID: 12139,  $\sim 60$  ks), on the 21st (ID: 11849,  $\sim 118$  ks), and on the 24th (ID: 12204,  $\sim 67$  ks). *XMM–Newton* observed the source again on 2013 January 17 for a total net exposure time of  $\sim 89$  ks. Both *XMM–Newton* observations (IDs: 0300240501 and 0694170101, respectively) were performed in ‘FULL WINDOW’ mode with the optical ‘THIN’ filter applied. Standard data reduction was made with the *SAS* v12.0.1 software for *XMM–Newton* and with the *CIAO* v4.5 software for *Chandra*. Observation-dependent redistribution matrices and ancillary responses were generated as standard for every data set. Spectral analysis was performed using the *XSPEC* v12.8.1 software (Arnaud 1996).

*XMM–Newton* European Photon Imaging Camera (EPIC) source products were extracted from source-centred circular regions, and the corresponding background ones were estimated from source-free nearby areas. For the sake of simplicity, and after having checked the good agreement among the pn, MOS1 and MOS2 data, only EPIC-pn spectra in the 0.5–10 keV band are used in this study. As for *Chandra*, we use the MEG data in the 1.2–7 keV band, and the HEG ones in the 1.4–9 keV. Outside these energy bands, the high-resolution spectra are background dominated. We used these spectra in two forms: (i) separately when interested on the short time-scale variability of the absorbers, and (ii) merged into one single  $\sim 291$  ks spectrum for each detector, representative of the broad-band X-ray continuum time-averaged over 10 d. The *XMM–Newton* spectra have been regrouped so that each bin contains 25 counts, while the *Chandra* spectra have been grouped to 4 channels per bin, and we use the  $\chi^2$  and *C*-statistic (Cash 1979) for the *XMM–Newton* and *Chandra* spectral analysis, respectively. Uncertainties correspond to the 90 percent confidence level for one interesting parameter, except if otherwise specified. Whenever fluxes were needed to be converted into luminosities, we have assumed a  $\Lambda$  cold dark matter ( $\Lambda$ CDM) cosmology with  $H_0 = 70 \text{ km s}^{-1} \text{ Mpc}^{-1}$ ,  $\Omega_\Lambda = 0.73$ , and  $\Omega_M = 0.27$ .

The X-ray spectra of the *XMM–Newton* and *Chandra* observations can be seen in Fig. 1. In order to facilitate comparison among them, all spectra have been divided by the effective area of each detector. Spectral variability on long time-scales is clearly present with absorption first decreasing between the first *XMM–Newton* observation (2006/02) and the *Chandra* one (2010/04) and then increasing significantly between the *Chandra* observation (2010/04) and the second *XMM–Newton* one (2013/01), as already studied in detail in our previous work on ESO 323–G77 (Miniutti et al. 2014).

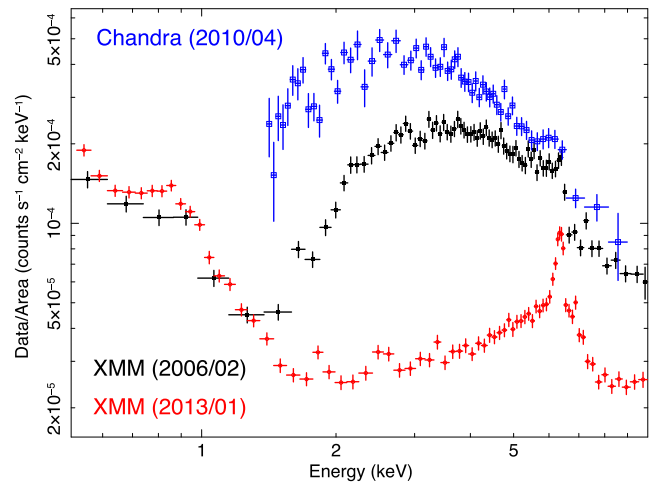


**Figure 1.** Long-term X-ray spectral variability of ESO 323–G77 as observed with *XMM–Newton* and *Chandra*. Only pn and HEG data, respectively, are shown for clarity. Data have been normalized to each detector effective area, and they have been rebinned for visual clarity.

## 3 THE TIME-AVERAGED 2010 CHANDRA SPECTRUM

We start our analysis by considering the merged MEG and HEG data from *Chandra*, i.e. we consider the time-averaged, high-resolution *Chandra* data that are representative of the spectrum between 2010 April 14 and the 24.

Based on our previous analysis of the source (Miniutti et al. 2014), we consider a baseline model comprising Galactic absorption (Kalberla et al. 2005), a power law X-ray continuum, a reflection continuum (Nandra et al. 2007) from neutral matter (with solar abundances and inclination fixed to an intermediate value of  $45^\circ$ ), and a scattered soft X-ray power law typical of obscured AGN (Matt et al. 2013). The photon indices of the nuclear continuum and of the soft scattered component are forced to be the same, while their normalizations are free to vary independently. The reflection model intensity is set by the so-called reflection fraction  $R$ , with the geometrical meaning that  $R = 1$  corresponds to the reflector covering half of the sky as seen by the irradiating source. The reflection model is convolved with a Gaussian kernel to account for any width of the associated emission lines (mainly Fe  $K\alpha$ ). As for the absorbing systems we include, as a first approximation, a neutral absorber fully covering the nuclear X-ray continuum. A constant is introduced to account for calibration uncertainties between the two detectors.

The best-fitting baseline model produces a statistical result of  $C = 2190$  for 1168 degrees of freedom (dof). The photon index is  $\Gamma = 1.85 \pm 0.06$ , and the X-ray continuum is absorbed by a column density of  $N_H = (3.3 \pm 0.2) \times 10^{22} \text{ cm}^{-2}$ . The soft scattered power law has a normalization that is about 4 per cent that of the nuclear X-ray continuum. The reflection fraction of the reflection model is  $R = 0.27 \pm 0.12$  and replacing the reflection model with a simple Gaussian emission line at  $\sim 6.4$  keV gives a line energy of  $6.39 \pm 0.02$  keV with equivalent width (EW) of  $50 \pm 10$  eV. The width of the line is in the range of 3–30 eV and corresponds to a full width at half-maximum (FWHM)  $\sim 330$ – $3300 \text{ km s}^{-1}$ , consistent with an origin in the BLR or further out (e.g. the so-called torus). In our analysis we fix the width of the Gaussian kernel applied to the neutral reflection model to an intermediate value of 10 eV.

**Table 1.** Absorption lines detected with Gaussian models in the time-averaged *Chandra* spectra from the MEG and HEG detectors. The phase label (first column) refers to the phase of the gas that is likely responsible for the specific absorption line and it is coded as follows: h = high-ionization warm absorber (with typical temperature in the range of  $10^6$ – $10^7$  K), l = low-ionization warm absorber ( $10^5$ – $10^6$  K), c = cold absorber ( $10^4$ – $10^5$  K). The last column is the statistical improvement associated with the corresponding Gaussian model. We gather all the atomic transitions data from the ATOMDB (Smith et al. 2001).

Phase	ID	Transition	$E_{\text{lab}}$ (keV)/ $\lambda_{\text{lab}}$ (Å)	$E_{\text{rest frame}}$ (keV)	–EW (eV)	$v_{\text{outflow}}$ (km s $^{-1}$ )	$\Delta C$
l+c	Ne x	1s $\rightarrow$ 4p	1.2770/9.708	1.283 $\pm$ 0.002	20 $\pm$ 4	1400 $\pm$ 450	40
l+c	Ne x	1s $\rightarrow$ 5p	1.3077/9.481	1.314 $\pm$ 0.002	15 $\pm$ 4	1450 $\pm$ 450	18
l+c	Mg xi	1s $^2$ $\rightarrow$ 1s2p	1.3522/9.169	1.359 $\pm$ 0.002	9 $\pm$ 5	1500 $\pm$ 450	11
l+c	Mg xii	1s $\rightarrow$ 2p	1.4723/8.421	1.480 $\pm$ 0.002	15 $\pm$ 3	1550 $\pm$ 400	71
c	Si viii	2p $^3$ $\rightarrow$ 1s 2s $^2$ 2p $^4$	1.7715/6.999	1.777 $\pm$ 0.002	13 $\pm$ 3	950 $\pm$ 300	28
c	Si ix	2p $^2$ $\rightarrow$ 1s 2s $^2$ 2p $^3$	1.7909/6.923	1.797 $\pm$ 0.002	12 $\pm$ 2	1000 $\pm$ 350	27
c	Si x	2p $\rightarrow$ 1s 2s $^2$ 2p $^2$	1.8084/6.856	1.816 $\pm$ 0.002	11 $\pm$ 3	1250 $\pm$ 350	24
l	Si xiii	1s $^2$ $\rightarrow$ 1s 2p	1.8650/6.648	1.875 $\pm$ 0.002	12 $\pm$ 2	1600 $\pm$ 300	63
l+h	Si xiv	1s $\rightarrow$ 2p	2.0056/6.182	2.017 $\pm$ 0.002	18 $\pm$ 2	1700 $\pm$ 300	181
l	Si xiv	1s $\rightarrow$ 3p	2.3765/5.217	2.388 $\pm$ 0.003	14 $\pm$ 3	1450 $\pm$ 350	25
l	S xv	1s $^2$ $\rightarrow$ 1s 2p	2.4605/5.039	2.473 $\pm$ 0.003	10 $\pm$ 3	1500 $\pm$ 400	17
l+h	S xvi	1s $\rightarrow$ 2p	2.6218/4.729	2.632 $\pm$ 0.003	11 $\pm$ 3	1150 $\pm$ 350	28
h	Fe xxv	1s $^2$ $\rightarrow$ 1s 2p	6.7019/1.850	6.73 $\pm$ 0.01	49 $\pm$ 7	1250 $\pm$ 450	41
h	Fe xxvi	1s $\rightarrow$ 2p	6.9650/1.780	6.99 $\pm$ 0.01	51 $\pm$ 9	1050 $\pm$ 450	36

The best-fitting continuum model reveals the presence of a series of relatively strong absorption lines in the 1.2–2.7 keV range and around 7 keV. We then add a series of Gaussian absorption lines to our best-fitting model. Each line is in principle associated with three free parameters, namely rest-frame energy, width, and intensity. After a few initial tests, we find that the width of most absorption lines cannot be well constrained by the data. In order to gain some insight on the typical line width, we select two of the strongest soft X-ray lines (at  $\sim$ 1.87 and  $\sim$ 2.02 keV at the galaxy redshift) and the two Fe absorption lines (at  $\sim$ 6.73 and  $\sim$ 6.99 keV), and we fit those lines with free Gaussian width. The two soft X-ray lines are both consistent with  $\sigma = 10 \pm 3$  eV, while the two highly ionized Fe lines have  $\sigma \leq 7$  eV. Hence, in the subsequent analysis, we fix the width of all Gaussian absorption lines to 10 eV, except that of the two highly ionized Fe lines which is instead fixed at 1 eV. Each Gaussian then only contributes with two free parameters (rest-frame energy and intensity). The relatively large width of the soft X-ray lines is likely an indication of turbulence and/or of a contribution of different gas phases with different velocities to most lines.

We detect a total of 14 absorption lines, each producing an improvement of  $\Delta C \geq 9.2$ , i.e. each line is associated with a statistical significance larger than  $\sim$ 99 per cent for the two free parameters. The final statistical result is of  $C = 1580$  for 1140 dof. In Table 1, we report the best-fitting parameters of the Gaussian absorption lines, as well as the corresponding identification and inferred outflow velocity. Errors on the lines parameters are computed using the STEPPAR command in XSPEC. The  $\Delta C$  improvement for each individual line is computed by removing the line under inspection from the best-fitting model and by re-fitting the data reaching a new best fit to be compared with the former.

As shown in Table 1, we can identify three main groups of absorption lines, likely associated with three different ionization states. The highest ionization phase (h) is associated with the Fe xxv and Fe xxvi absorption lines, with possible contributions to Si xiv and S xvi. An intermediate ionization state (l) is probed mainly by Si xiii, Si xiv, and S xv with other possible contribution at Ne x, Mg xi, and Mg xii, as well as at S xvi. Finally, a series of Si absorption lines (Si viii–x) is associated with a colder phase (c), which may also contribute, together with the intermediate ionization phase, at Ne x, Mg xi, and Mg xii.

According to our lines ID in Table 1, all phases have similar outflow velocities (of the order of 1000–2000 km s $^{-1}$ ), although excluding lines that may be associated with more than one single phase, the high ionization (h) and the cold phase (c) may be slightly slower than the intermediate zone (l).

### 3.1 A global absorption model

In order to reproduce the absorption features that are present in the data, we start our analysis by applying two ionized absorbers to the nuclear continuum, which is already absorbed by a neutral column of  $\sim 3 \times 10^{22}$  cm $^{-2}$ . We use the photoionization code PHASE, developed by Krongold et al. (2003). PHASE assumes a simple geometry that consists of a central source emitting an ionizing continuum with clouds of gas intercepting the LOS, in a plane parallel approximation. The ionization balance is calculated using CLOUDY (last described in Ferland et al. 2013). In this case, we use a simple power-law spectral energy distribution (SED) with photon index  $\Gamma = 2$  over the whole Lyman continuum. The SED is normalized to the historical 2–10 keV luminosity of ESO 323–G77 (Miniutti et al. 2014). This SED is shown in red in Fig. 2, and denoted by (u) for *unabsorbed*. We also include in the same figure another SED that will be defined and used later in this section. The parameters of the code are (1) the ionization parameter defined as  $U = Q(4\pi n R^2 c)^{-1}$  (Netzer 2008), where  $Q$  is the photon rate integrated over the entire Lyman continuum,  $n$  is the gas number density, and  $R$  the gas distance from the nuclear source of photons, (2) the equivalent hydrogen column density, (3) the outflow velocity, and (4) the internal microturbulent velocity. The electron temperature in the models presented here corresponds to the photoionization equilibrium of the gas.

The two ionized absorbers provide a large statistical improvement with respect to the baseline continuum model reaching  $C = 1591$  for 1160 dof (to be compared with  $C = 2190$  for 1168) and the best-fitting parameters are reported in Table 2 (Model 1). The data and best-fitting model are shown in the left-hand panels of Fig. 3. Although the model represents a significant statistical improvement, some of the absorption lines we detect with Gaussian models (see Table 1) are only poorly reproduced. This is particularly true for some Si lines between 1.7 and 1.8 keV (observed-frame) as seen

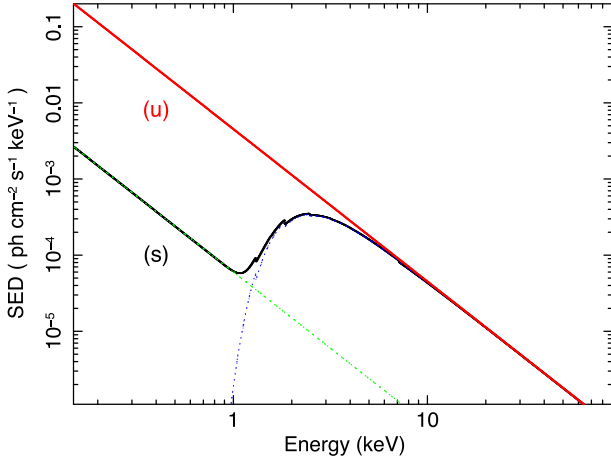


**Figure 2.** The unabsorbed (u) and soft–X-rays-absorbed (s) SED used in this work are shown as solid lines (upper and lower lines, respectively) in a restricted X-ray regime. The overall SED can be obtained with a simple extrapolation between 1 Ry and infinity. In the (s) case the two main spectral components are also shown, namely the soft scattered power law and the absorbed nuclear continuum which dominate the spectrum below and above  $\sim 1$  keV, respectively.

in the second left-hand panel of Fig. 3, for the S XV line around 2.4 keV (third left-hand panel), and for the Fe XXVI line that is only poorly accounted for (bottom left-hand panel). Some residuals are also left at the softest X-ray energies (see top left-hand panel of Fig. 3), although they seem to have lower significance.

In our model, the series of Si lines around 1.8 keV are all due to the low-ionization l-phase ( $\log U \sim -0.3$ , see Model 1 in Table 2), while the strong Si XIV and S XVI lines are exclusively produced by the high-ionization h-phase together with the Fe lines ( $\log U \sim 1.5$ ).

Increasing the ionization of this hotter phase to better reproduce the Fe XXVI line decreases the strength of the Si XIV and S XVI ones, and worsens the fitting statistics because the l-phase is not hot enough to contribute there. This would be possible only increasing as well the ionization of the l-phase, but then the other Si lines would not be reproduced, as they are associated with lower ionization.

The only sensible solution seems that of introducing a cold phase which may account for the Si lines around 1.8 keV allowing the ionization of the other two components to increase and to better reproduce the Si XIV, S XV, S XVI, and Fe XXVI lines. It would obviously be possible to simply introduce a third PHASE component. However, the ionization is likely to be low, so that we consider the possibility of replacing the cold absorber that characterizes our continuum model with a low-ionization absorber. Hence we replace the neutral absorber (so far modelled with the ZPHABS model in XSPEC) with a third PHASE component.

Replacing the neutral absorber with a third PHASE component produces a statistically significant improvement, and the best fit reaches  $C = 1433$  for 1157 dof (to be compared with  $C = 1591$  for 1160 dof, obtained with two ionized and one strictly neutral absorber). The best-fitting parameters are reported in Table 2 (Model 2). The data and best-fitting model are shown in the right-hand panels of Fig. 3. The best-fitting models are shown in the left-hand panels of Fig. 4 in the two energy bands where the most relevant features are imprinted (a soft X-ray band up to  $\sim 2.7$  keV is shown in the upper panel, and the Fe K region in the lower).

As expected, the ionization of the two absorbers of our previous model significantly increases. The h-phase is now characterized by  $\log U \sim 1.9$ , while the l-phase has  $\log U \sim 0.5$ . Now, the Si XIV and S XVI lines are well reproduced with contribution from both absorbers, while the high-ionization phase accounts very well for both the Fe XXV and Fe XXVI lines. The l-phase also accounts better for the S XV absorption feature around 2.4 keV. On the other hand, the

**Table 2.** Best-fitting parameters for the time-averaged MEG and HEG *Chandra* data. Column densities are expressed in  $\text{cm}^{-2}$ , the ionization parameter  $U$  is dimensionless by definition, while  $\xi$  is in units of  $\text{erg cm s}^{-1}$ . The different columns are characterized by the different models for the absorbers. The symbol ‘n’ represents a strictly neutral absorber, ‘u’ and ‘s’ represent ionized absorbers modelled with the unabsorbed (u) or soft-absorbed (s) SED in PHASE, and ‘i’ an ionized absorber modelled with the XSTAR-based model ZXIPCF. The superscript <sup>f</sup> means that the parameter has been fixed, while the symbol ‘P’ indicates that it reached the model upper/lower limit, respectively.

		Model 1 u×u×n	Model 2 u×u×u	Model 3 s×s×u	Model 4 i×i×i
	$\Gamma$	$1.85 \pm 0.06$	$1.96 \pm 0.05$	$1.95 \pm 0.05$	$2.15 \pm 0.07$
Warm abs.	h-phase				
	$\log U$	$1.5 \pm 0.1$	$1.9 \pm 0.2$	$0.0 \pm 0.2$	–
	$\log \xi$	–	–	–	$4.1 \pm 0.1$
	$\log N_{\text{H}}$	$23.2 \pm 0.1$	$23.4 \pm 0.2$	$23.3 \pm 0.2$	$23.7 \pm 0.2$
	$v_{\text{turb}}$	$600\text{--}900^{\text{P}}$	$600\text{--}900^{\text{P}}$	$600\text{--}900^{\text{P}}$	$200^{\text{f}}$
l-phase	$v_{\text{outflow}}$	$1500 \pm 200$	$1100 \pm 200$	$1200 \pm 200$	$800 \pm 200$
	$\log U$	$-0.3 \pm 0.1$	$0.5 \pm 0.1$	$-1.0 \pm 0.1$	–
	$\log \xi$	–	–	–	$2.7 \pm 0.2$
	$\log N_{\text{H}}$	$22.50 \pm 0.08$	$22.41 \pm 0.09$	$22.49 \pm 0.08$	$22.5 \pm 0.1$
	$v_{\text{turb}}$	$500\text{--}900^{\text{P}}$	$600\text{--}900^{\text{P}}$	$600\text{--}900^{\text{P}}$	$200^{\text{f}}$
Cold abs.	$v_{\text{outflow}}$	$1400 \pm 200$	$1750 \pm 200$	$1700 \pm 200$	$1850 \pm 200$
	c-phase				
	$\log U$	–	$-0.45 \pm 0.05$	$-0.56 \pm 0.05$	–
	$\log \xi$	–	–	–	$1.6 \pm 0.2$
	$\log N_{\text{H}}$	$22.20 \pm 0.06$	$22.70 \pm 0.04$	$22.59 \pm 0.05$	$22.9 \pm 0.2$
	$v_{\text{turb}}$	–	$600 \pm 200$	$600 \pm 200$	$200^{\text{f}}$
	$v_{\text{outflow}}$	–	$1400 \pm 300$	$1300 \pm 300$	$1500 \pm 300$
	$C/\text{dof}$	1591/1160	1433/1157	1413/1157	1700/1160

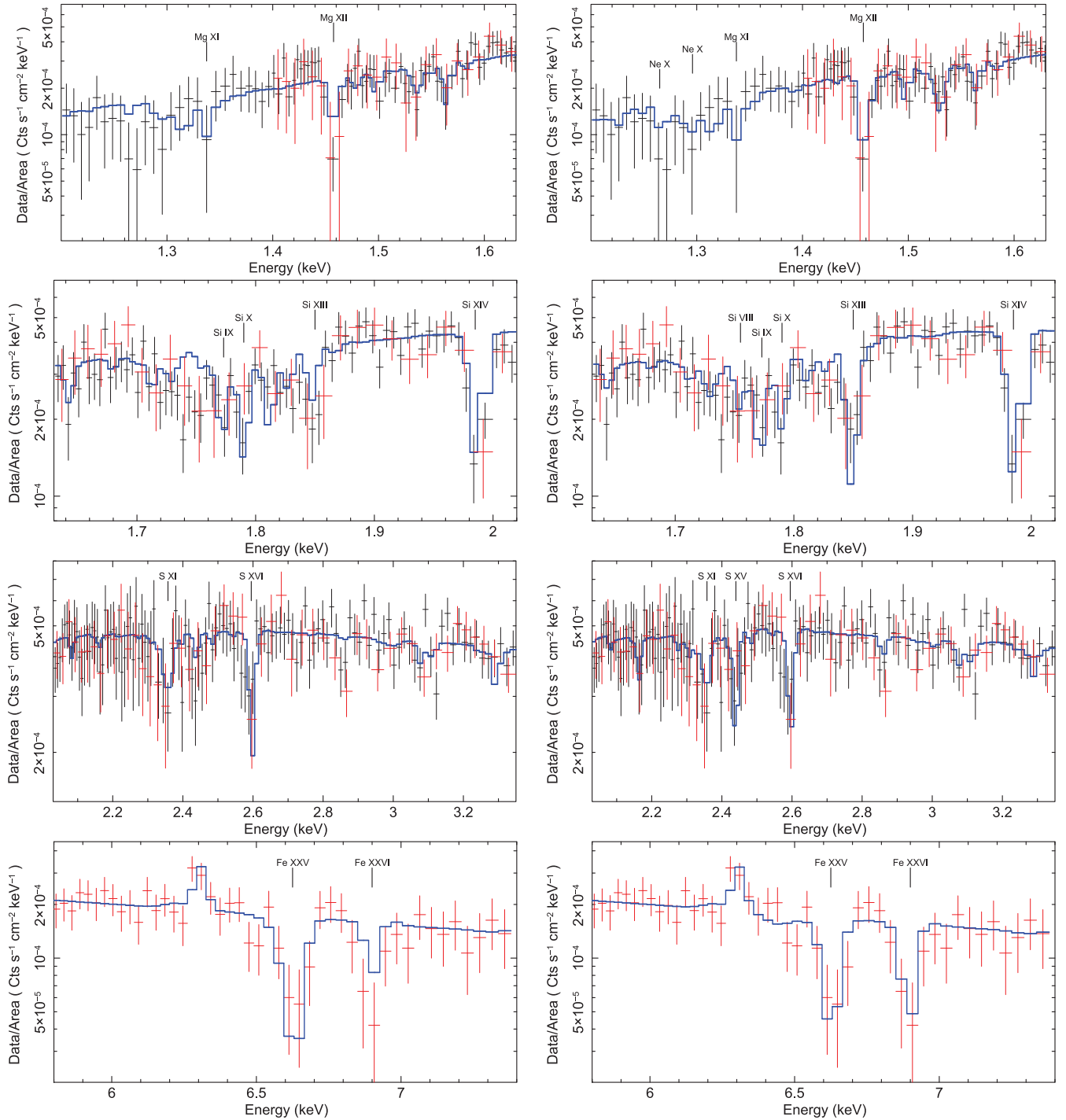


**Figure 3.** We show the area-corrected MEG (black) and HEG (red) data and best-fitting models in four energy bands (from top to bottom they are 1.2–1.63, 1.63–2.05, 2.05–3.35, and 5.8–7.4 keV). We omit the intermediate 3.35–5.8 keV band as no strong lines are seen in this range. The left-hand panels refer to Model 1 in Table 2 (namely two ionized and one neutral absorbers), and the right-hand panels refer to Model 2 (three ionized absorbers). The best-fitting model (solid line) is only that convolved with the MEG response in the three top panels, while only HEG data and model are shown in the bottom panels to ensure simplicity and visual clarity.

new, colder absorber ( $\log U \sim -0.45$ ) accounts for the Si complex around 1.8 keV (and also slightly improves the fit at the lowest energies, where Ne and Mg lines are detected, see Table 1). All the improvements of Model 2 with respect to Model 1 can be seen in the comparison between left-hand (Model 1) and right-hand (Model 2) panels of Fig. 3.

We measure a non-zero velocity for all phases. The outflow velocities are of  $1100 \pm 200 \text{ km s}^{-1}$  for the h-phase, of  $\sim 1750 \pm 200 \text{ km s}^{-1}$  for the l-phase, and of  $1400 \pm 300 \text{ km s}^{-1}$  for the coldest absorber (c-phase). The l-phase appears to be faster than the other two. This is consistent with the results reported in Table 1 where it was shown that lines associated with the h-phase only (the

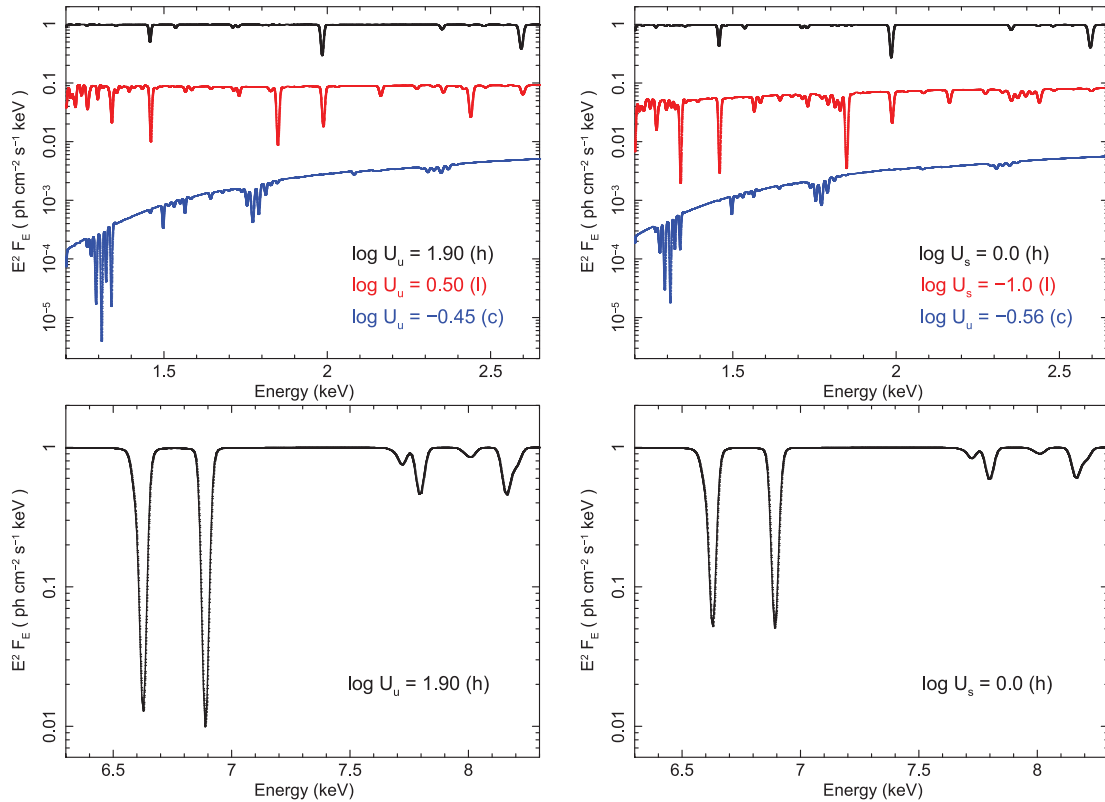


**Figure 4.** In the top panels we show the best-fitting models for the three PHASE components in the soft X-ray band between 1.2 and 2.65 keV (where the strongest features are seen). The bottom panels show the Fe K region, where the only significant contribution is from the highly ionized component. The models are all applied to a power law with  $\Gamma = 2$  and are rescaled by factors of 10 in order to avoid confusion. The left-hand panels refer to Model 2 in Table 2 ( $u \times u \times u$  configuration), where all absorbers see the same, unabsorbed SED ( $u$ ). The right-hand panels are for Model 3 ( $s \times s \times u$  configuration), where the h- and l-phases see a SED that is absorbed by a neutral column of  $3 \times 10^{22} \text{ cm}^{-2}$  ( $s$ ), while the c-phase sees the unabsorbed SED ( $u$ ). As can be seen, the two models differ slightly in some of the line ratios, while the general structure is the same. In particular, the l-phase is always responsible for higher ionization lines than the c-phase despite the nominally lower  $U$  obtained with Model 3 (right-hand panels).

Fe lines) and those associated with the c-phase only (the Si VIII to Si X lines) have velocities in the range of 900–1300 km s<sup>-1</sup>, while lines associated with the l-phase only (such as Si XIII and S XV) have marginally higher velocity (1300–1800 km s<sup>-1</sup>). As for the turbulent velocities, the only one that can be constrained is that of the coldest component which is  $v_{\text{turb}}^{(c)} = 600 \pm 200 \text{ km s}^{-1}$ . Only lower limits are obtained for the other two phases with  $600 \leq v_{\text{turb}}^{(l,h)} \leq 900 \text{ km s}^{-1}$  (note that the PHASE code only allows for  $v_{\text{turb}} \leq 900 \text{ km s}^{-1}$ ).

As mentioned, we have so far used a common SED (a simple power law with photon index 2 over the whole Lyman continuum) for the three absorbers. This SED is represented with the symbol  $u$  for *unabsorbed* in Table 2. However, as can be seen in the top left-hand panel of Fig. 4, the cold component affects the spectral shape significantly in the soft X-rays. If the cold absorber is located closer to the nuclear source than the other phases, the h- and l-phase would see a different, absorbed SED. To explore the possible effects of such a scenario, we introduce a new SED, namely we consider the same nuclear power law with  $\Gamma = 2$  as before, but absorbed by a column density of  $3 \times 10^{22} \text{ cm}^{-2}$  of cold gas (representative of the effect of the c-phase). In the soft X-rays (and below), this new SED is therefore dominated by the soft, scattered power law which is always present. The luminosity of the soft power law is  $L_{0.5-2} = 6.7 \times 10^{40} \text{ erg s}^{-1}$  while, as already mentioned, that of the nuclear continuum is the historical average for ESO 323–G77 ( $L_{2-10} = 5.8 \times 10^{42} \text{ erg s}^{-1}$ ). Both luminosities are from Miniutti et al. (2014). This absorbed SED is represented with the symbol ‘s’

for *soft X-rays absorbed* in Table 2, and is shown in black in Fig. 2 in order to ease comparison with the unabsorbed SED. The relation between the integrated photon rate  $Q$  for the unabsorbed SED ( $u$ ) and the new, soft-X-ray-absorbed SED ( $s$ ) is  $Q_u \simeq 50 Q_s$ . The introduction of this new model enables us to explore the possibility that the c-phase is closer to the nuclear source than the other two (or at least cospatial with them), thus reducing the irradiating flux on the h- and l-phases. As the two warm/hot phases see the absorbed SED, while the c-phase still sees the unabsorbed one, the model is called  $s \times s \times u$ , as opposed to the case in which all phases see the same unabsorbed SED which is called  $u \times u \times u$ .

Repeating the analysis in the  $s \times s \times u$  configuration produces a relatively marginal improvement and gives  $C = 1413$  for the same number of dof as in the  $u \times u \times u$  explored above (which gave  $C = 1433$ ) and results are reported in Table 2 as Model 3. We believe that the  $\Delta C$  between the two models is not sufficiently large to prefer one solution over the other on firm statistical grounds, but we take it as an indication that the c-phase is either more internal or at least cospatial with the other two, rather than more external.

Note that the ionization parameter of the two higher ionization warm absorbers drops significantly with  $\Delta \log U = \log U_u - \log U_s = 1.9 \pm 0.4$  for the h-phase and  $1.5 \pm 0.2$  for the l-phase. This mostly reflects the change in ionizing photon rate  $Q$  due to the reduction of the SED at soft X-rays; indeed, both  $\Delta U$  are consistent with the expected relation between the ionization parameters of the two different SED, namely  $\Delta \log U = \Delta \log Q = \log(Q_u Q_s^{-1}) \simeq 1.7$ .

A marginal drop of the ionization of the c-phase is also seen despite an identical SED, but we must stress that fixing the ionization of the  $s \times s \times u$  model to be the same as in the  $u \times u \times u$  case, the fitting statistics is only marginally worse ( $\Delta C = 5$ ), so that an acceptable solution with the same ionization for the cold phase does exist.

According to the ionization parameters of the three absorbers in the  $s \times s \times u$  (Model 3), one would assume that the l-phase (with  $\log U \simeq -1.0$ ) is now colder than the c-phase ( $\log U \simeq -0.6$ ). However, the two ionization parameters cannot be directly compared, as they are associated with two different SED. In fact, the l-phase is still responsible for higher ionization lines than the c-phase. This is shown in the right-hand panels of Fig. 4 showing the best-fitting PHASE models associated with the  $s \times s \times u$  configuration (Model 3). Comparing the right-hand panels of Fig. 4 with its left-hand panels (which are associated with the  $u \times u \times u$  configuration, i.e. with Model 2), it is clear that the best-fitting models for all three phases are only marginally different, despite the h- and l-phases have very different ionization parameters, and that the l-phase is always responsible for higher ionization lines than the c-phase.

As a last step, in order to ease comparisons with other works/sources when using different photoionization models, we consider the XSTAR-based ZXIPCF model in XSPEC and repeat the analysis by using three ZXIPCF component instead of the three PHASE ones. The free parameters of the ZXIPCF model are the ionization parameter, defined as  $\xi = L/(nr^2)$  where the luminosity is integrated between 1 and 1000 Ry, the column density, and the outflow velocity. As for the turbulent velocity, it is fixed to 200 km s<sup>-1</sup> in the model. The intrinsic SED is a slightly steeper power law of  $\Gamma = 2.2$  than for the PHASE model we used so far ( $\Gamma = 2.0$ ).

The ZXIPCF-based model (Model 4 in Table 2) is a significantly worse description of the data than the equivalent  $u \times u \times u$  model based on the PHASE code (Model 2 in Table 2). This is mostly due to a worse description of the ionized Fe absorption lines that are only partially reproduced by the model. Moreover the softest X-ray energies (where Ne and Mg lines dominate) are not well reproduced, and residuals are also seen around 1.8 keV (mostly Si lines). The best-fitting ionization parameters are significantly higher than those of Model 2. This is expected because of the different definition of ionization parameters. In fact, assuming the same 2–10 keV luminosity for the two SED (one with  $\Gamma = 2$ , and the other with  $\Gamma = 2.2$ ), the conversion between the ZXIPCF ionization parameter and  $U$  is  $\log \xi = 1.99 + \log U$ . Indeed, the ionization parameters derived with the ZXIPCF-based Model 4 and those derived via the PHASE-based Model 2 are all consistent with that conversion within the errors (see Table 2). Besides the different treatment of atomic physics, one further possible reason for the worse description of the data with Model 4 with respect to Model 2 is that the ZXIPCF model assumes a relatively modest turbulent velocity of 200 kms, while the best-fitting parameters in Model 2 suggest a much higher  $v_{\text{turb}}$ . Hence, we do not discuss any further the ZXIPCF model and we consider to have reached a satisfactory description of the *Chandra* time-averaged spectrum with Model 2 (or Model 3).

The resulting picture is the following: during the  $\sim 10$  d corresponding to the time-averaged *Chandra* spectrum, the X-ray continuum in ESO 323–G77 is transmitted through three absorbers, ionized at different degrees. Although there is a slight difference in the statistical results from the two physical scenarios defined above (Model 2 and Model 3 in Table 2), we cannot claim a highly significant preference for one of the two scenarios. For simplicity, we adopt here the  $u \times u \times u$  Model 2. This choice allows us to compare directly the ionization parameters of the absorbers, as they all see the same SED. Moreover, as discussed above, there is no loss of

generality because all parameters of Model 3 can be obtained from those of Model 2 simply rescaling the ionization parameters taking into account the different photon rate  $Q$ .

In this context, we characterize the warm absorbers (h- and l-phases) as two structures with ionization parameters of  $\log U^{(h)} \simeq 1.9$  and  $\log U^{(l)} \simeq 0.5$ , and equivalent hydrogen column densities of the order of a few  $\times 10^{23}$  and a few  $\times 10^{22}$  cm<sup>-2</sup>, respectively. The third absorber, previously thought to be neutral, turns out to be ionized, with  $\log U^{(c)} \simeq -0.45$  and a column density of few  $\times 10^{22}$  cm<sup>-2</sup>. As per the outflow velocities, there are no striking differences among the three ionization phases, and the most likely physical scenario appears to be one in which the warm absorbers and the coldest one are all part of an outflow characterized by velocities in the range of  $\sim 1000$ – $2000$  km s<sup>-1</sup>, although the l-phase appears to be marginally faster than the other two phases.

#### 4 SHORT TIME-SCALE ABSORBERS VARIABILITY

Having reached a fair description of the time-averaged *Chandra* data, we are now able to focus on the specific differences among the four *Chandra* observations performed during 10 d in 2010 April. We start by applying the best-fitting model described above (Model 2 in Table 2) to the four *Chandra* observations. The continuum photon index is initially free to vary but, as no variability is seen after a few tests, it is forced to be the same in all observations. On the other hand, the continuum normalization is free to vary independently.

We initially force all absorbers parameters to be the same in all observations and we perform a joint fit to the four observations. This is done to obtain a benchmark result that will be used to assess the significance of any absorber variability once parameters will be let free to vary independently in each observation. We reach a statistical result of  $C = 5351$  for 4673 dof. All parameters are consistent, within the errors, with those obtained from the time-averaged spectrum (Table 2) and they are given in the upper part of Table 3.

In order to explore any absorber variability, we then leave the ionization and column density of the three phases free to vary independently in the four observations, while keeping constant outflow and turbulent velocities for each phase (this assumption turns out to be justified by an a posteriori check which shows no improvement if these parameters are allowed to vary). The new best-fitting result is  $C = 5273$  for 4655 dof. The improvement is exclusively due to the variability of the c-phase ionization. All other parameters are consistent with remaining constant in the four observations, as shown in the middle part of Table 3.

We then perform a final fit where all parameters are forced to be the same in the four observations except the c-phase ionization (i.e. the only parameter that is significantly variable). This is done to derive the  $\Delta C$  that is obtained when only the c-phase ionization is free to vary. We obtain  $C = 5289$  for 4670 dof, i.e. an improvement by  $\Delta C = 62$  for 3 dof with respect to the benchmark model (all absorbers forced to be constant). This demonstrates that the variability of the c-phase ionization is highly significant, and that a constant ionization can be safely excluded. The best-fitting parameters for this model are reported in the lower part of Table 3.

In order to gain some insights on the origin of the observed variability, we consider here the relationship between the absorber ionization and the 2–10 keV nuclear luminosity. Under the assumption of no intrinsic variation of the SED shape between the four *Chandra* observations (as it is the case, since the photon index is consistent with being constant) and of the gas density and location,

**Table 3.** Best-fitting results for the analysis of the four 2010 *Chandra* observations from April 14 to April 24 considered separately. The continuum photon index is initially free to vary but, after testing for its lack of variability, it is forced to be the same in all observations ( $\Gamma = 1.97 \pm 0.06$ ). In the upper part of the table, we show the best-fitting results obtained if all the absorbers parameters are forced to be the same at all epochs (i.e. we reproduce the results obtained using the time-averaged spectrum, see Table 2 for comparison). The middle part of the table shows results obtained when the ionization and column density of the three absorbing phases are free to vary independently in each of the four observations while keeping, for each phase, common outflow and turbulent velocities. Finally, the lower part of the table shows results obtained by forcing all absorbers parameters to be the same at all epochs except the c-phase ionization, which is the only one that varies significantly. As it was the case for the time-averaged *Chandra* spectra, the turbulent velocity of the h- and l-phases is  $\geq 600 \text{ km s}^{-1}$  (with a model upper limit of  $900 \text{ km s}^{-1}$ ) while, in all fits, the c-phase is characterized by a turbulent velocity of  $600 \pm 200 \text{ km s}^{-1}$ . Units are the same as in Table 2. The symbol ‘p’ means that the parameter reached the limit allowed by the model.

Obs. date	$\log U$	h-phase $\log N_{\text{H}}$	$v_{\text{outflow}}$	$\log U$	l-phase $\log N_{\text{H}}$	$v_{\text{outflow}}$	$\log U$	c-phase $\log N_{\text{H}}$	$v_{\text{outflow}}$
All phases forced to be constant at all epochs ( $C/\text{dof} = 5351/4673$ )									
	$2.1 \pm 0.3$	$23.7^{+0.3\text{p}}_{-0.3}$	$1200 \pm 200$	$0.5 \pm 0.1$	$22.40 \pm 0.09$	$1800 \pm 300$	$-0.44 \pm 0.05$	$22.70 \pm 0.05$	$1450 \pm 250$
All phases allowed to vary in ionization and column density ( $C/\text{dof} = 5273/4655$ )									
April 14	$2.0 \pm 0.4$	$23.7^{+0.3\text{p}}_{-0.3}$	$1250 \pm 250$	$0.5 \pm 0.2$	$22.2 \pm 0.2$	$1800 \pm 350$	$-0.30 \pm 0.08$	$22.7 \pm 0.1$	$1500 \pm 250$
April 19	$2.1 \pm 0.4$	$23.8^{+0.2\text{p}}_{-0.4}$	$1250 \pm 250$	$0.5 \pm 0.2$	$22.3 \pm 0.2$	$1800 \pm 350$	$-0.60 \pm 0.09$	$22.7 \pm 0.1$	$1500 \pm 250$
April 21	$2.1 \pm 0.4$	$23.8^{+0.2\text{p}}_{-0.4}$	$1250 \pm 250$	$0.5 \pm 0.1$	$22.4 \pm 0.2$	$1800 \pm 350$	$-0.45 \pm 0.08$	$22.7 \pm 0.1$	$1500 \pm 250$
April 24	$2.1 \pm 0.4$	$23.6^{+0.4\text{p}}_{-0.2}$	$1250 \pm 250$	$0.6 \pm 0.1$	$22.5 \pm 0.2$	$1800 \pm 350$	$-0.34 \pm 0.09$	$22.7 \pm 0.1$	$1500 \pm 250$
All phases forced to be the same at all epochs, except the c-phase ionization ( $C/\text{dof} = 5289/4670$ )									
April 14	$2.1 \pm 0.3$	$23.7^{+0.3\text{p}}_{-0.3}$	$1200 \pm 200$	$0.5 \pm 0.1$	$22.40 \pm 0.09$	$1800 \pm 300$	$-0.31 \pm 0.04$	$22.70 \pm 0.05$	$1450 \pm 250$
April 19	$2.1 \pm 0.3$	$23.7^{+0.3\text{p}}_{-0.3}$	$1200 \pm 200$	$0.5 \pm 0.1$	$22.40 \pm 0.09$	$1800 \pm 300$	$-0.56 \pm 0.07$	$22.70 \pm 0.05$	$1450 \pm 250$
April 21	$2.1 \pm 0.3$	$23.7^{+0.3\text{p}}_{-0.3}$	$1200 \pm 200$	$0.5 \pm 0.1$	$22.40 \pm 0.09$	$1800 \pm 300$	$-0.48 \pm 0.06$	$22.70 \pm 0.05$	$1450 \pm 250$
April 24	$2.1 \pm 0.3$	$23.7^{+0.3\text{p}}_{-0.3}$	$1200 \pm 200$	$0.5 \pm 0.1$	$22.40 \pm 0.09$	$1800 \pm 300$	$-0.36 \pm 0.04$	$22.70 \pm 0.05$	$1450 \pm 250$

the X-ray luminosity is proportional to the photon rate  $Q$  that enters the definition of ionization parameter  $U = Q(4\pi cnR^2)^{-1}$ , i.e. doubling the luminosity implies that  $Q$  and therefore  $U$  is twice as large (as the SED is a simple power law, the luminosity can be considered in any arbitrary band). Hence, we do expect a linear relationship between ionization  $U$  and luminosity if the absorbing gas phase is in photoionization equilibrium with the ionizing continuum. We consider the  $U$ – $L_{2-10}$  relationship instead of the  $U$ – $Q$  one, because we prefer to use two direct observables.

As can be seen in Table 3, the ionization of the h- and l-phases is consistent with being constant during the 10 d probed by the *Chandra* observations. However, the relatively large errors imply that the two parameters could also be linearly related to  $L_{2-10}$  at the same significance level, so that no information can be obtained for the two warm/hot phases. Hence, we focus here on the c-phase only, which is the only one showing significant ionization variability. Fig. 5 shows the c-phase ionization as a function of the 2–10 keV X-ray luminosity (in log–log space). The shaded area is the range of  $\log U$  obtained when all absorbers parameters (including the c-phase ionization) are forced to be the same at all epochs (see upper part of Table 3), while data points are those reported in the lower part of the same table. The solid line represents the best-fitting relation of the form  $\log U = a \log L_{2-10} + b$ , where  $a$  is fixed to unity to show that a linear relationship between  $U$  and  $L_{2-10}$  is indeed consistent with the data. The tilted dashed lines represent the associated uncertainty (at the 99 per cent confidence level). Letting  $a$  free to vary confirms the linear relation although with relatively large error ( $a = 1.1 \pm 0.4$ ) and excludes, as expected, the case of constant  $U$  ( $a = 0$ ).

We then conclude that the observed variability is driven by the linear response of the c-phase ionization to variations of the intrinsic luminosity (or photon rate  $Q$ ). This strongly suggests that the c-phase is dense enough to be in photoionization equilibrium with

the irradiating nuclear source on time-scales as short as a few days. As mentioned, the h- and l-phase are consistent with both constant ionization and with a linear relationship between  $U$  and X-ray luminosity, so that no information is gained in those cases. Repeating the analysis with the  $s \times s \times u$  configuration (i.e. assuming Model 3 of Table 2 as baseline instead of Model 2) gives very similar results, and only the c-phase ionization is significantly variable (and satisfies again a linear relationship between  $U$  and  $L_{2-10}$ ).

## 5 THE 2006 AND 2013 XMM–NEWTON OBSERVATIONS

The best-fitting models reached in the previous sections characterize the ionization states, equivalent column densities, and outflow velocities of three absorbers (all ionized at different degrees, and all with similar outflow velocities), based on the rich set of absorption lines detected in 2010 with *Chandra*. Here, we refine our results as far as possible adding data from *XMM–Newton* observations of 2006 and 2013 (pn) that have been previously studied by Jiménez-Bailón et al. (2008) and Miniutti et al. (2014), respectively.

The resolution of the *Chandra* HETGS is much greater than that of *XMM–Newton* EPIC-pn instrument, so that the pn spectra do not show the profusion of lines that the HEG/MEG spectra do [as discussed by Miniutti et al. (2014) the Reflection Grating Spectrometer (RGS) data do not offer enough spectral quality to be discussed in any of the available *XMM–Newton* observations]. However, in order to try to assess the variability of the absorbers detected with *Chandra*, we consider here the *XMM–Newton* pn spectra from the 2006 and 2013 observations.

The relatively simple baseline continuum model used so far is not an adequate description of the *XMM–Newton* data. This is for two main reasons: (i) the *XMM–Newton* data extend down to 0.5 keV

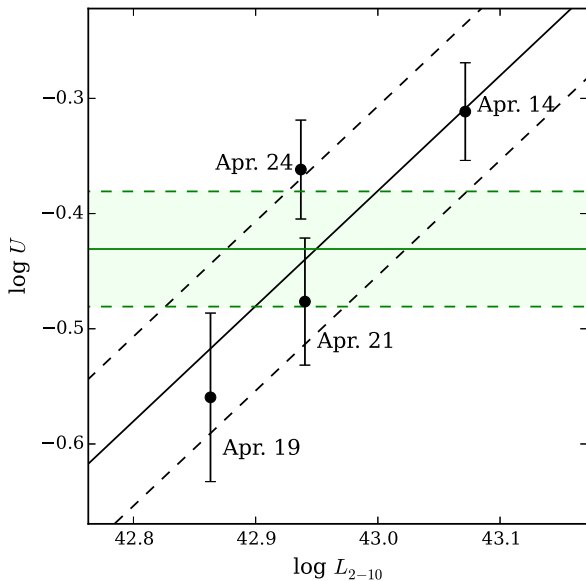


**Figure 5.** The ionization of the c-phase component is shown as a function of the 2–10 keV X-ray luminosity in log–log space. The shaded area between horizontal dashed lines is the best-fitting interval obtained when  $U$  is forced to be the same at all epochs (see upper part of Table 3). The data correspond to the case where all absorbers parameters, except the c-phase ionization, are kept constant between the four *Chandra* observations (lower part of Table 3). The tilted solid line is the best-fitting linear relation between  $U$  and  $L_{2-10}$ , i.e.  $\log U = a \log L_{2-10} + b$  with  $a$  fixed to unity, and the tilted dashed lines represent the statistical fitting error given here at the 99 per cent confidence level. This shows that the data are consistent with a linear relation between  $U$  and  $L_{2-10}$ , as expected if the gas is in photoionization equilibrium with the irradiating continuum. Letting  $a$  free to vary confirms the linear relation although with relatively large error ( $a = 1.1 \pm 0.4$ ). Note that some changes in gas properties (or intrinsic SED) may be present between April 21 and 24, which would explain the slightly different ionization of the c-phase despite an almost identical luminosity.

(as opposed to the *Chandra* data that do not have sufficient signal-to-noise ratio below 1.2 keV) and reveal structure in the soft X-rays, and (ii) the *XMM-Newton* observations (especially the 2013 one) are more heavily absorbed than the *Chandra* one (see e.g. Fig. 1) and an additional hard X-ray component is visible in the heavily absorbed 2013 *XMM-Newton* spectrum.

As discussed extensively by Miniutti et al. (2014), the soft X-ray structure is well reproduced by adding two thermal plasma components (the *APEC* model in *XSPEC*) to the soft power law which represents the scattered re-emission of the nuclear continuum by some extended gas. On the other hand, the 2013 *XMM-Newton* spectrum requires an additional power law in the hard X-ray band, absorbed by a column density that is different from that affecting the nuclear emission. This component was interpreted by Miniutti et al. (2014) as scattered emission in a clumpy absorber. The idea is that, if the main absorber is clumpy instead of homogeneous, the observed spectrum should comprise not only a transmitted component (i.e. the nuclear continuum absorbed by the particular clump that happens to be in our LOS) but also a scattered component due to clumps out of the LOS that intercept the nuclear emission re-directing part of it into the LOS. As this scattered component reaches us after passing through the clumpy absorber itself, it is absorbed by the spatially averaged column density of the clumps rather than by that of the particular one that is in the LOS at the given epoch. This explains why the scattered component is absorbed by a different column

density than the nuclear continuum, although the scattered fraction (i.e. basically the ratio between the scattered and nuclear luminosity) and the column density towards the scattered component should be the same at all epochs (as they represent spatially averaged values). Miniutti et al. (2014) have derived a scattered fraction of  $15 \pm 3$  per cent and a (neutral) column density of  $(7.6 \pm 0.8) \times 10^{22} \text{ cm}^{-2}$  towards the scattered component. Note that the scattered component makes a non-negligible contribution to the hard X-ray spectrum only when the nuclear continuum is sufficiently absorbed (i.e. for column densities significantly higher than  $7 \times 10^{22} \text{ cm}^{-2}$ ), which only occurs during the 2013 *XMM-Newton* observation.

We then consider a new baseline continuum model comprising all the above components. The global baseline model and its main components are shown in fig. 3 of Miniutti et al. (2014). We first perform a joint fit to the two *XMM-Newton* observations and we force all parameters that are not expected to vary between the two epochs to be the same, namely (i) the temperature and normalization of the two *APEC* components, (ii) the photon index and normalization of the soft scattered power law, (iii) the column density towards the hard scattered power law as well as the hard scattered fraction, and (iv) the flux of the neutral reflection component (carrying the Fe  $K\alpha$  emission line). The best-fitting model produces  $\chi^2 = 1649$  for 1445 dof. Close inspection of the Fe  $K\alpha$  region reveals the presence of some emission structure bluewards of the line, especially in the more heavily absorbed 2013 *XMM-Newton* observation. We add a Gaussian emission line forcing it to have the same properties in the two observations and we reach  $\chi^2 = 1612$  for 1443 dof for an additional Gaussian emission line at  $6.50 \pm 0.04 \text{ keV}$  (in the galaxy rest frame). When the line intensity is allowed to vary between the two observations, no improvement is obtained, and the line EW is  $\sim 35 \text{ eV}$  in 2006 and  $\sim 85 \text{ eV}$  in 2013, reflecting the lower X-ray continuum in 2013. If no energy shift is assumed, the line most likely arises from ionized Fe emission.

All parameters that are kept in common between the two observations are reported in Table 4. As for the variable parameters, they are the nuclear continuum photon index and normalization, and the (neutral) column density towards it. As already shown by Miniutti et al. (2014), the 2006 *XMM-Newton* observation is absorbed by a column of  $\sim 5.6 \times 10^{22} \text{ cm}^{-2}$ , while the column density during the 2013 observation is one order of magnitude higher. The two photon indices are consistent with each other within the errors ( $\Gamma = 1.95 \pm 0.07$  in 2006 and  $2.0 \pm 0.1$  in 2013).

Having derived a baseline continuum model for the two observations, we now search for signatures of absorption features. All common parameters are fixed to their best-fitting values obtained from the joint fit of the two observations (see Table 4) and we consider the two observations separately. The baseline model (with common parameters fixed at their best-fitting values) results in  $\chi^2 = 829$  for 705 dof for the 2006 observation and  $\chi^2 = 783$  for 749 dof for the 2013 one. We first add a series of Gaussian absorption lines with width fixed at 1 eV and redshift fixed at the galaxy one, and we report the lines improving the fit by more than  $\Delta\chi^2 = 9.2$  in Table 5 together with their possible identification for the 2006 and 2013 observations.

### 5.1 The 2006 *XMM-Newton* observation

The two more significant lines are detected at  $6.75 \pm 0.03$  and  $7.06 \pm 0.04 \text{ keV}$ . If identified with Fe  $\text{xxv}$  and Fe  $\text{xxvi}$ , respectively, the observed lines are associated with high outflow velocities and, considering the large errors, with a possible common outflow velocity of  $3100 \pm 400 \text{ km s}^{-1}$ . This outflow velocity is significantly

**Table 4.** Best-fitting common parameters for the simultaneous broad-band analysis of the 2006 and 2013 *XMM–Newton* observations. Luminosities are in units of  $10^{42}$  erg  $s^{-1}$ , temperatures and energies are given in keV, the column density is in units of  $10^{22}$   $cm^{-2}$ , and the line intensity is given in units of  $10^{-6}$  photons  $s^{-1}$   $cm^{-2}$ . For parameters that are different between the two observations (nuclear continuum photon index and luminosity as well as its column density), see text.

Common constant components in the 2006/2013 <i>XMM–Newton</i> observations					
Soft scatt.	APEC (1)		APEC (2)		
$L_{0.5-2}$	$kT$ (keV)	$L_{0.5-2}$	$kT$ (keV)	$L_{0.5-2}$	
$(6.7 \pm 0.3) \times 10^{-2}$	$0.80 \pm 0.04$	$(2.8 \pm 0.2) \times 10^{-2}$	$0.09 \pm 0.03$	$(9 \pm 1) \times 10^{-3}$	
Cold refl.	Hard scatt.		Ionized Fe line		
$L_{2-10}$	$L^{\text{scatt}}/L^{\text{nucl}}$	$N_{\text{H}}$	$E_{\text{rest}}$	Intensity	
$0.31 \pm 0.02$	$0.14 \pm 0.03$	$7.5 \pm 0.8$	$6.50 \pm 0.04$	$5.3 \pm 1.7$	

**Table 5.** Absorption lines detected with Gaussian models in the *XMM–Newton* EPIC-pn spectra. Every line contributes with two free parameters (rest-frame energy and intensity). Only lines producing a statistical improvement of  $\Delta\chi^2 \geq 9.2$  are reported.

Phase	ID	Transition	$E_{\text{lab}}$ (keV)/ $\lambda_{\text{lab}}$ (Å)	$E_{\text{rest frame}}$ (keV)	–EW (eV)	$v_{\text{outflow}}$ (km $s^{-1}$ )	$\Delta\chi^2$
2006 <i>XMM–Newton</i> observation							
h	S <small>XXVI</small>	1s $\rightarrow$ 2p	2.6218/4.729	$2.64 \pm 0.03$	$20 \pm 10$	$2050 \pm 3350$	10
h	Fe <small>XXV</small>	1s <sup>2</sup> $\rightarrow$ 1s2p	6.7019/1.850	$6.75 \pm 0.03$	$80 \pm 20$	$2150 \pm 1300$	44
h	Fe <small>XXVI</small>	1s $\rightarrow$ 2p	6.9650/1.780	$7.06 \pm 0.04$	$90 \pm 20$	$4050 \pm 1350$	37
–	–	–	–	$7.7 \pm 0.1$	$60 \pm 30$	–	11
–	–	–	–	$8.4 \pm 0.1$	$60 \pm 30$	–	11
2013 <i>XMM–Newton</i> observation							
–	–	–	–	$2.15 \pm 0.03$	$40 \pm 15$	–	18

higher than that derived from the *Chandra* data from the same two absorption lines (which have a common outflow velocity of  $1150 \pm 350$  km  $s^{-1}$ ). The absorption line at  $\sim 2.64$  keV (see Table 5) is not highly significant, and can be probably associated with S XXVI, although the very large error on the line energy does not allow to place a secure label on this feature. If the line is indeed associated with S XXVI, the outflow velocity is consistent with that of the two ionized Fe lines (although with large error), possibly indicating a common origin in a highly ionized wind. The other two, less significant absorption lines in the 2006 observation have no clear identification (see Table 5).

The detection of Fe XXV and Fe XXVI absorption lines means that a hot phase with similar ionization as that detected in 2010 with *Chandra* is present in the 2006 observation as well, so we replace all Gaussian absorption lines with a PHASE model. The PHASE model produces a significant improvement, and we reach  $\chi^2 = 712$  for 701 dof (to be compared with  $\chi^2 = 829$  for 705 dof of the baseline continuum model). The absorber has  $\log U = 2.0 \pm 0.3$ , a column density of  $\log N_{\text{H}} \geq 23.4$ , and an outflow velocity of  $2700 \pm 1100$  km  $s^{-1}$ , consistent within the relatively large error with the common outflow velocity of  $3100 \pm 400$  km  $s^{-1}$  derived from the energy shift of the Fe XXV and Fe XXVI absorption lines.

As can be seen in Table 5, we do not find any absorption line that may be related to the l- or c-phases detected in the high-resolution *Chandra* data. However, it is interesting to see if gas with similar properties as seen in the 2010 *Chandra* observation is consistent with the 2006 *XMM–Newton* data as well. We first add an l-phase, fixing all of its parameters to those detected with *Chandra* (see Table 2, Model 2). The statistical result ( $\chi^2 = 710$  for 701 dof) cannot be distinguished from the one with no l-phase ( $\chi^2 = 712$  for the same number of dof). Letting all the parameters of the l-phase free to vary does not produce any improvement. We conclude that gas with the same properties as the l-phase detected with *Chandra*

in 2010 is neither required nor excluded by the *XMM–Newton* data. Its non-detection is likely due to (i) the worse energy resolution of the pn data, and (ii) the higher column density of the coldest phase which lowers significantly the signal-to-noise ratio in the relevant spectral region (starting to be dominated by extended emission and scattered light rather than by the X-ray nuclear continuum).

As for the strictly neutral absorber (with column density of  $\sim 5.6 \times 10^{22}$   $cm^{-2}$ ), we replace it with an ionized PHASE model. As no absorption lines associated with that component are detected, we fix its outflow velocity to that detected with *Chandra*, namely 1400 km  $s^{-1}$  (see Model 2 in Table 2). The replacement, however, does not produce any improvement, and the resulting ionization parameter is only an upper limit of  $\log U \lesssim -0.3$ . Hence, a non-zero ionization of the coldest phase is neither required nor excluded by the *XMM–Newton* data. The column density of this coldest phase presents some degree of degeneracy with the (basically unconstrained) ionization parameter and can take any value between  $\log N_{\text{H}} \simeq 22.7$  and  $\log N_{\text{H}} \simeq 23.3$  (the lower column density being associated with the lowest possible ionization,  $\log U = -3$ ).

However, as shown in the previous section, the c-phase ionization responds to the continuum variations on short time-scales during the 2010 *Chandra* 10-d-long monitoring, and this response can be used to break the degeneracy between ionization and column density in the 2006 data. This is because, assuming a perfectly homogeneous c-phase even on long time-scales (i.e. no clumpiness for the c-phase) the 2006 ionization can be predicted from the 2010 one by considering the different intrinsic continuum luminosity at the two epochs. For a fixed SED shape (and the photon indices in 2006 and 2010 are consistent with each other), the 2–10 keV X-ray intrinsic luminosity is proportional to the photon rate  $\dot{Q}$  and hence to the ionization state  $U$ . As the c-phase ionization during the 2010 *Chandra* observation is  $\log U = -0.45$  (see Model 2 in Table 2) and since the intrinsic 2–10 keV luminosity in 2006 is a factor of  $\sim 1.3$

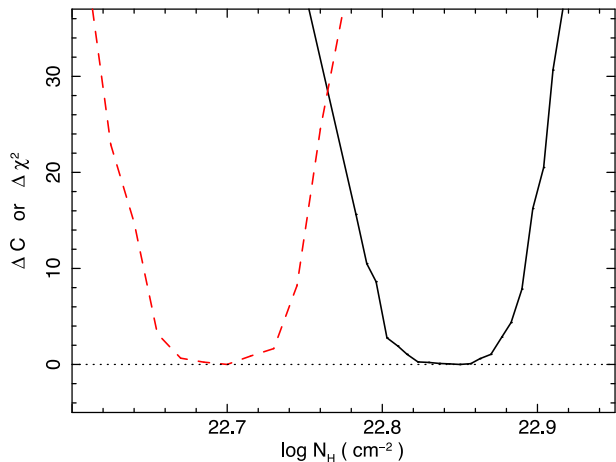


**Figure 6.** The statistical improvement as a function of the c-phase column density for the 2010 *Chandra* (left) and the 2006 *XMM-Newton* (right) observations as obtained with the `STEPPAR` command in `XSPEC`. We use the  $\Delta C$  and  $\Delta\chi^2$  values for the *Chandra* and the *XMM-Newton* data, respectively. All parameters are free to vary during the minimization except the ionization of the c-phase during the 2006 *XMM-Newton* observation. This ionization is fixed to that expected under the assumption of a homogeneous rather than clumpy absorber ( $\log U = -0.56$ , see text for details). The column densities of the c-phase at the two epochs are similar but inconsistent with each other at more than  $5\sigma$ , strongly suggesting the inhomogeneous nature of the c-phase.

lower than in 2010, the 2006 c-phase must have ionization  $\log U = -0.56$  if the c-phase is homogeneous (as opposed to clumpy) on long time-scales.

This removes the degeneracy between column density and ionization during the 2006 *XMM-Newton* observation, and allows us to check whether the absorber is indeed homogeneous as opposed to clumpy, by comparing the 2006 and 2010 column densities directly. This comparison is shown in Fig. 6 in terms of the statistical improvement as a function of column density for the 2010 (left) and 2006 (right) observations. Although the difference is small in absolute terms, the two column densities are inconsistent with each other at more than  $5\sigma$ , indicating the non-homogeneous nature of the c-phase absorber on long time-scales. A clumpy absorber is also strongly suggested by the presence of a hard scattered component during the much more heavily absorbed 2013 *XMM-Newton* observation as discussed in detail by Miniutti et al. (2014).

We do not replace the neutral absorber towards the hard scattered component with an ionized one because this component has an almost negligible contribution in the 2006 *XMM-Newton* observation and it is only strictly required by the 2013 *XMM-Newton* data (Miniutti et al. 2014).

The best-fitting parameters for our final model, comprising the highly ionized h-phases and the two neutral absorbers towards the continuum and the hard scattered component, are reported in Table 6. Fig. 7 (top) shows the high-energy spectrum from the 2006 observation together with our best-fitting model, dominated by the Fe emission lines at 6.4 and  $\sim 6.5$  keV, and by the h-phase component.

## 5.2 The 2013 *XMM-Newton* observation

The only significant absorption line detected in the 2013 *XMM-Newton* spectrum is at  $\sim 2.15$  keV (see Table 5). Its identification is difficult, and we also note that the feature occurs close to where a

**Table 6.** Best-fitting parameters for the *XMM-Newton* observations. For the 2006 observation, the two c-phases are here modelled with a strictly neutral absorber at rest, as no improvement is obtained by replacing them with a `PHASE` model (see text for details on the parameters obtained when an ionized model is used instead). The superscript <sup>f</sup> means that the parameter is fixed, the symbol <sup>p</sup> indicates that the error on one parameter reached the limit of the model. Units as in Table 2.

		2006	2013	
Warm abs.	h-phase	$\Gamma$	$1.95 \pm 0.07$	$2.0 \pm 0.1$
		$L_{2-10}^{\text{nucl}}$	7.5	5.8
		$\log U$	$2.0 \pm 0.3$	$2.0 \pm 0.3$
		$\log N_{\text{H}}$	$23.7^{+0.3p}_{-0.3}$	$23.6^{+0.4p}_{-0.4}$
		$v_{\text{turb}}$	100–900	100–900
		$v_{\text{outflow}}$	$2700 \pm 1100$	$4100 \pm 1700$
Cold abs.	c-phase	$\log U$	–	$0.2 \pm 0.2$
		$\log N_{\text{H}}$	$22.7 \pm 0.2$	$23.8 \pm 0.1$
		$v_{\text{turb}}$	–	100–900
		$v_{\text{outflow}}$	$0^f$	$1400^f$
Scatt. abs.	c-phase	$\log U$	–	$\lesssim -0.3$
		$\log N_{\text{H}}$	$22.9^f$	$22.9 \pm 0.2$
		$v_{\text{turb}}$	–	100–900
		$v_{\text{outflow}}$	$0^f$	$1400^f$
		$\chi^2/\text{dof}$	712/701	754/739

significant drop in quantum efficiency is seen for the pn detector, so that we cannot exclude that it has an instrumental origin. Hints for high-energy absorption lines bluewards of the Fe  $K\alpha$  emission line are seen, but none reaches the required  $\Delta\chi^2 = 9.2$  when Gaussian models are considered.

With no absorption lines, applying detailed photoionization codes to the 2013 data will likely result in overmodelling. However, the nuclear and scattered continua are still absorbed by strictly neutral matter, while from the *Chandra* observations, we have indications that even the coldest component is in fact ionized. Note also that, based on the long-term variability properties of the coldest absorber, Miniutti et al. (2014) have interpreted the 2013 data with absorption from a cloud of the BLR as opposed to the 2006 *XMM-Newton* and 2010 *Chandra* observations where the c-phase was associated with a clumpy absorber at the torus scale.

We test this scenario in the following way: we first replace the neutral absorber towards the nuclear continuum with a `PHASE` model. The lack of absorption features means that we are unlikely to be sensitive to outflow velocities, and we choose to fix it to the 2010 c-phase outflow velocity ( $1400 \text{ km s}^{-1}$ ). The model produces  $\chi^2 = 772$  for 747 dof, slightly better than the baseline ( $\chi^2 = 783$  for 749 dof). We obtain  $\log U^{\text{nucl}} \sim 0.2$  with  $\log N_{\text{H}}^{\text{nucl}} \sim 23.8$  for the c-phase towards the nuclear continuum. Hence, the main absorber in 2013 is significantly more highly ionized than that in 2006 and 2010 (as well as being associated with a much higher column density). As for the hard scattered component absorber, replacing it with a `PHASE` model outflowing at  $1400 \text{ km s}^{-1}$  does provide a very marginal improvement ( $\chi^2 = 768$  for 743 dof), but its ionization is only an upper limit of  $\log U^{\text{scatt}} \lesssim -0.3$ . Letting the outflow velocities of the two absorbers free to vary does not provide any improvement, and the large errors are consistent with zero velocity (as well as with velocities of a few thousands  $\text{km s}^{-1}$  in both outflow and inflow), showing that we are not sensitive to this parameter, as expected.

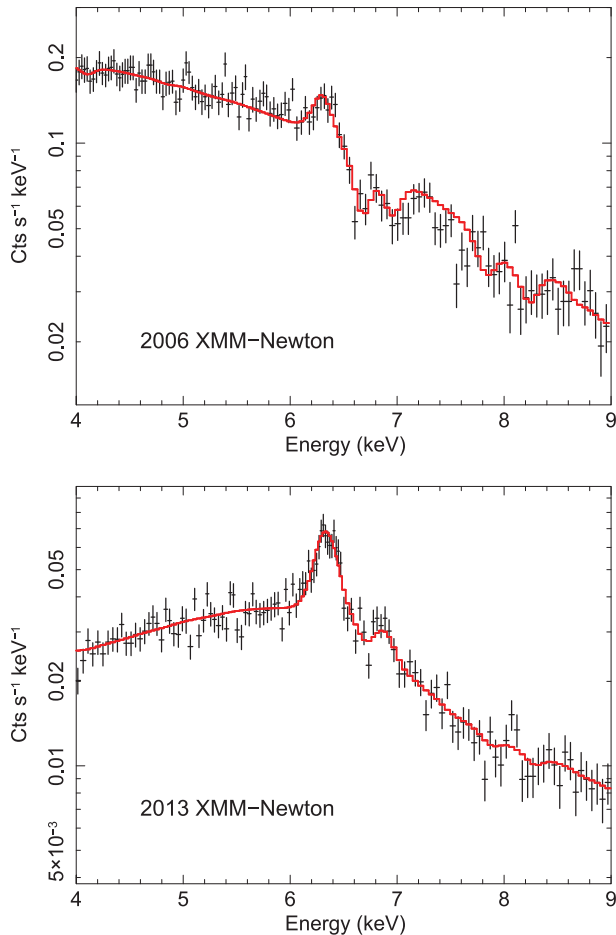


**Figure 7.** The high-energy part of the *XMM-Newton* EPIC-pn spectra from the 2006 (top) and 2013 (bottom) observations is shown together with the best-fitting model. The high-energy absorption features are well reproduced by the h-phase, although the significance of this component is relatively low in the 2013 data. The improvement of the statistical result with the addition of the h-phase is  $\Delta\chi^2 = 117$  for 4 dof in the 2006 data and only  $\Delta\chi^2 = 14$  in the 2013 data. Data have been slightly rebinned for visual clarity.

As some hints for high-energy absorption lines are seen in the data, we add a highly ionized PHASE component to assess whether the h-phase can be detected in the 2013 *XMM-Newton* data. In this case, we leave the outflow velocity free to vary, as it may be possible to constrain it if a set of low EW absorption features is present in the data (although none is individually significant). We reach a best fit of  $\chi^2 = 754$  for 739 dof, marginally better than that with no h-phase component ( $\chi^2 = 768$  for 743 dof). The h-phase has  $\log U \sim 2.0$ ,  $\log N_{\text{H}} \sim 23.6$ , and an outflow velocity of  $4100 \pm 1700 \text{ km s}^{-1}$ . As it was the case for the 2006 *XMM-Newton* observation adding an l-phase with the same properties as that detected in 2010 with *Chandra* neither improve nor worsen the best fit. Hence such a component is not required by the data, but its presence cannot be excluded either. Our final best-fitting parameters are reported in Table 6 and the high-energy spectrum from the 2013 observation is shown in the bottom panel of Fig. 7, where the (low significance) h-phase imprints some weak absorption features.

Summarizing, the 2006 observation shows a clear h-phase with ionization and column density of the order of those detected with the high-resolution *Chandra* data (note, however, that its outflow velocity is significantly higher). Although the 2006 data do not allow us to distinguish between a strictly neutral and an ionized

c-phase, we have shown that the 2006 c-phase column density is most likely different from the 2010 one, strongly suggesting that the c-phase is not homogeneous on long time-scales, but rather most likely clumpy.

In 2013, the nuclear continuum is absorbed by a much higher column (close to  $10^{24} \text{ cm}^{-2}$ ) of higher ionization gas ( $\log U \sim 0.2$ ), and a low-significance h-phase is detected with similar properties to that observed in 2006. The heavily absorbed 2013 X-ray spectrum reveals the presence of a hard scattered component. The scattered fraction is  $\sim 14$  per cent, and the scattered emission is transmitted through a gas phase with  $\log U \lesssim -0.3$  and  $\log N_{\text{H}} \sim 22.9$ . A phase with intermediate ionization is not required by the 2006 and 2013 *XMM-Newton* data, but an l-phase with the same properties as that detected with *Chandra* in 2010 is consistent with both data sets.

## 6 DISCUSSION

The temperature and ionization state of the three absorbers we have detected with *Chandra* are similar to those of warm absorbers typically detected in Seyfert 1 galaxies. Column densities are however on the high side for standard warm absorbers, see e.g. Torresi et al. (2010) or Gupta et al. (2013). Moreover, the column density of the coldest absorbing system is of the same order, or even higher, than that of the higher ionization components while, in general, higher ionizations are associated with larger columns (e.g. Zhang et al. 2015). These differences can be interpreted naturally within a scenario in which ESO 323–G77 represents a source intermediate between Seyfert 1 and Seyfert 2 galaxies. In fact, considering the polar-scattered nature of the source, and its likely intermediate inclination of  $\sim 45^\circ$  (Schmid et al. 2003), ESO 323–G77 appears to lie precisely in that intermediate-inclination region of the parameter space. In this framework, the cold absorber we detect would be the same warm absorber as seen in other sources, with its special properties due to the orientation at which we are seeing this source: grazing the edge of the clumpy torus. Objects observed at higher inclination angles (with respect to the symmetry axis) than ESO 323–G77 correspond to highly X-ray obscured Seyfert 2 galaxies; sources viewed at slightly lower inclination angles are typical Seyfert 1 galaxies with standard warm absorbers; objects at even lower inclination angles result into a Seyfert 1 optical classification and are likely to be characterized by the absence of warm absorbers (i.e. polar Seyfert 1 galaxies offering a naked view of the innermost X-ray emitting region).

The three absorbers we detect in the high-resolution *Chandra* data have similar outflow velocities, suggesting a common origin. Only the coldest one responds with ionization changes to intrinsic luminosity variations on short time-scales (days). The coldest absorber is most likely clumpy, as suggested by the comparison between the column densities derived in 2010 and in 2006, and by the need for an extra hard scattered component in the heavily absorbed 2013 observation, as discussed already by Miniutti et al. (2014). On the other hand, the highest ionization phase is consistent with the same ionization and column density on both short and long time-scales, although its outflow velocity appears to be variable on long time-scales. As for the intermediate zone (the l-phase), it is only detected in the high resolution, relatively unobscured *Chandra* observation. However, a phase with similar properties is allowed (not required) to be present in the *XMM-Newton* data as well. This suggests that the warm absorbers are distributed in a more homogeneous way than the coldest one. Such properties (similar outflow velocities, clumpiness of the denser, colder absorber, and relatively homogeneous distribution of the warmer phases) suggest to

consider a solution in which all absorbers are part of the same outflow, with the warmer phases providing the pressure confinement that is necessary to support relatively long-lived, dense, colder clouds [although originally considered for the BLR case, see e.g. Krolik, McKee & Tarter (1981) for the multiphase confinement model, and Emmering, Blandford & Shlosman (1992) and Elvis (2000) for the idea of an outflowing multiphase structure of the BLR].

Such a scenario cannot be directly confirmed by the data, but we can at least test whether the three absorbers detected in the 2010 *Chandra* observation are consistent with being in pressure equilibrium. In order to derive the properties of the three gas phases, we need to estimate the product  $nR^2$  which, by definition, only depend on the ratio between photon rate and ionization ( $Q/U$ ). This means that deriving the gas properties from the  $u \times u \times u$  configuration (Model 2 in Table 2) or from the  $s \times s \times u$  one (Model 3) gives the same result (we have shown in Section 3.1 that, for the h- and l-phases, the drop in  $U$  obtained with Model 3 is simply proportional to the drop in  $Q$  due to the different, absorbed SED). For simplicity, as well as for consistency with the previous sections, we continue to use the  $u \times u \times u$  configuration (Model 2) as best-fitting model from which we derive estimates on the gas properties. As mentioned, consistent results are obtained using Model 3 instead.

### 6.1 The ‘cold’ absorber in 2010

We proceed with orders-of-magnitude estimates of the properties of the absorbing gas. According to our best-fitting model (Model 2 in Table 2), the photon rate integrated from 1 Ry to infinity is  $Q \simeq 1.8 \times 10^{53}$  photons  $s^{-1}$  during the 10 d probed by the *Chandra* time-averaged spectrum.

From the fact that the cold absorber is in photoionization equilibrium with the impinging continuum within 5 d, as shown in Fig. 5, and using the formula and procedures of Nicastro, Fiore & Matt (1999) with the recombination time-scales and fractions for Si VIII- $x$  for the best-fitting ionization parameter  $\log U^{(c)} = -0.45$ , one can estimate a lower limit on the cold absorber number density of  $n^{(c)} \gtrsim 5 \times 10^4$   $cm^{-3}$  (using other ions produces a difference of a few per cent only). Using the definition of  $U$ , one has that  $R^{(c)} \lesssim 5 \times 10^{18}$  cm  $\simeq 1.6$  pc. A lower limit on the location of the c-phase can be obtained by considering that the observed outflow velocity ( $\sim 1400$  km  $s^{-1}$ ) cannot be lower than the escape velocity at the minimum launching radius. Knowing that the black hole mass is  $M_{BH} \simeq 2.5 \times 10^7 M_{\odot}$  (Wang & Zhang 2007), we derive  $R^{(c)} \gtrsim 3 \times 10^{17}$  cm  $\simeq 0.1$  pc. Note that the dust sublimation radius in ESO 323–G77 is located at  $\sim 0.14$  pc (Miniutti et al. 2014), so that the c-phase is consistent with being located somewhere between the inner and outer edges of the so-called torus (Krolik & Kriss 2001). This conclusion agrees well with that reached by e.g. Blustin et al. (2005) who, based on the analysis of high energy-resolution data on a sample of 23 AGN, have shown that warm absorbers most likely originate as outflows from the dusty torus.

Using again the definition of ionization parameter, the lower limit on  $R^{(c)}$  translates into an upper limit on the number density, namely  $n^{(c)} \lesssim 10^7$   $cm^{-3}$ . Finally, using derived values of  $n^{(c)}$ , the observed column density  $\log N_H^{(c)} \simeq 22.7$ , and assuming a spherical absorbing cloud, the diameter of the cloud  $D^{(c)}$  is in the range of  $[5 \times 10^{15} - 10^{18}]$  cm. Having constrained the absorber density and knowing its equilibrium temperature (which is  $\sim 5 \times 10^4$  K according to our best-fitting PHASE model), the pressure of this component can be estimated as  $P = k_B n T$  (where  $k_B$  is the Boltzmann constant), so that  $P^{(c)} = [3 \times 10^{-7} - 7 \times 10^{-5}]$  dyne  $cm^{-2}$ .

### 6.2 The two warm absorbers in 2010

In order to check if the warm/hot absorbers can pressure-confine the clumpy coldest phase, we assume here co-spatiality of the three phases, as suggested by the similar outflow velocities. Hence, for all absorbers, we assume  $R = [0.3 - 5] \times 10^{18}$  cm. Using  $Q \simeq 1.8 \times 10^{53}$  photons  $s^{-1}$  and the best-fitting ionization parameters of the h- and l-phases ( $\log U^{(h)} \simeq 1.9$  and  $\simeq 0.5$ ), one can constrain the number densities of the two warm absorbers to be  $n^{(h)} = [2 \times 10^2 - 7 \times 10^4]$   $cm^{-3}$  and  $n^{(l)} = [6 \times 10^3 - 2 \times 10^6]$   $cm^{-3}$ , respectively. According to our best-fitting model, the temperature of the two warm absorbers is  $5.8 \times 10^6$  K for the h-phase and  $5.5 \times 10^5$  K for the l-phase, so that their pressure is  $P^{(h)} = [10^{-7} - 6 \times 10^{-5}]$  dyne  $cm^{-2}$  and  $P^{(l)} = [4 \times 10^{-7} - 10^{-4}]$  dyne  $cm^{-2}$ , respectively. The pressure of the warm absorbers is in both cases consistent with that derived for the c-phase. The common pressure interval for the three phases to be in pressure equilibrium is  $P^{(c,h,l)} = [4 \times 10^{-7} - 6 \times 10^{-5}]$  dyne  $cm^{-2}$ .

We then conclude that the wind we detect in the data from the 2010 *Chandra* observations is consistent with being associated with the atmosphere of the clumpy torus, and with being arranged in three phases in pressure equilibrium with each other, with the coldest clumps being confined by the more homogeneous and hotter phases. Note that we cannot claim that both the h- and l-phases contribute to the confinement, but only that they are both consistent with this role which may be well dominated by one of the two phases.

### 6.3 The absorbers in 2006 and 2013

The ionization of the c-phase is only poorly constrained during the 2006 *XMM-Newton* observation. However, its column density is clearly higher than that during the 2010 *Chandra* observation, demonstrating the clumpiness of this component. The truly different case is represented by the 2013 *XMM-Newton* observation, where a much higher column density and ionization for the c-phase are obtained. As mentioned, Miniutti et al. (2014) have interpreted the c-phase in 2013 as due to a clump (cloud) of the BLR, as opposed to the 2010 (and probably 2006) observations where we just show that the c-phase is most likely associated with the clumpy torus.

We first assume that the 2013 c-phase has the same origin as in 2006 and 2010, namely that it is confined within the inner and outer edges of the torus. According to our best-fitting model, the photon rate in the 2013 *XMM-Newton* observation is  $Q \simeq 10^{53}$  photons  $s^{-1}$  and the best-fitting ionization of the cold phase is  $\log U \simeq 0.2$ . Hence, if the 2013 absorber was co-spatial with the c-phase detected in 2010 with *Chandra*, its density should be  $\sim 8$  times lower than in 2010 ( $(Q/U)^{(2013)} \simeq (Q/U)^{(2010)}/8$ ). Given the much higher column density observed in 2013 ( $N_H^{(2013)} \simeq 12.6 N_H^{(2010)}$ ), the 2013 absorbing cloud should be larger in size by a factor of  $\sim 100$  with respect to the 2010 absorber. Since the 2010 absorber has an estimated diameter larger than  $5 \times 10^{15}$  cm, the 2013 cloud would have a diameter of at least  $5 \times 10^{17}$  cm. Even assuming the highest possible orbital velocity for the range of radii associated with the torus ( $\sim 1100$  km  $s^{-1}$ ), a cloud of that size would cover a negligibly small X-ray emitting region for about 140 yr.

The X-ray history of ESO 323–G77 excludes that this is the case, as variability associated with column density of the order of that observed during the 2013 observation do occur on time-scales as short as 1 month, as demonstrated by Miniutti et al. (2014) using *Swift* data. In order to produce such short time-scale variability, any absorber must be smaller and denser by orders of magnitude, which places the 2013 absorber much closer in, in a region of the

parameter space that is roughly consistent with the dust-free BLR (note, however, that the 2013 absorber is not necessarily associated with a cloud that produces the optical broad lines, as its ionization parameter is likely too high to produce the correct line ratios). Moreover, if the 2013 absorber were associated with the dusty torus, UV variability between 2006 and 2013 would have been expected, due to the dramatic increase in column density. However, as reported by Miniutti et al. (2014), no decrease in UV fluxes was detected in 2013 despite the increase in the X-ray column density by about one order of magnitude, which strongly suggests that the 2013 c-phase is dust-free and thus part of the BLR rather than of the dusty torus. We then conclude that while the 2006 cold absorber is most likely part of the same clumpy absorbing structure as in 2010 (at spatial scales consistent with the dusty, clumpy torus), the 2013 absorber is more consistent with being associated with a denser and dust-free clump of the BLR, in line with the ones detected, for example, in NGC 1365 (Risaliti et al. 2009a), SWIFT J2127.4+5654 (Sanfrutos et al. 2013), or Mrk 335 (Longinotti et al. 2013).

On the other hand, the h-phase has similar ionization and column density in all observations, but its outflow velocity appears to be higher in the 2006 and 2013 *XMM–Newton* observations than in the 2010 *Chandra* one. This may indicate that this highly ionized phase is also somewhat clumpy, or that it is more efficiently accelerated when the X-ray continuum is suppressed by c-phase absorption (the *Chandra* observation being the less absorbed).

## 7 SUMMARY AND CONCLUSIONS

We present results from six observations of the polar-scattered Seyfert 1.2 galaxy ESO 323–G77. Four observations were taken by the HETGS on board *Chandra* within 10 d in 2010 April. Two more observations were taken with *XMM–Newton* and are considered here for comparison. The first one, obtained in 2006, is slightly more absorbed than the *Chandra* one. The second (2013) is much more heavily absorbed (see e.g. Fig. 1).

The high-resolution *Chandra* data are characterized by a rich set of absorption lines that can be associated with three outflowing absorbing gas phases with different ionizations. A highly ionized phase (h-phase) is responsible for the Fe<sub>XXV</sub> and Fe<sub>XXVI</sub> absorption lines and it also contributes to the observed Si<sub>XIV</sub> and S<sub>XVI</sub> features. An intermediate-ionization zone (l-phase) is mostly revealed by Si<sub>XIII–XIV</sub> and S<sub>XV–XVI</sub>, and contributes as well at low energies where absorption due to Ne<sub>X</sub> and Mg<sub>XI–XII</sub> is seen. A third, low-ionization phase (c-phase) is also detected and accounts for the Si<sub>VIII–X</sub> lines while contributing, together with the l-phase, at Ne<sub>X</sub> and Mg<sub>XI–XII</sub> as well. The latter phase replaces the strictly neutral absorber that is ubiquitously observed in Compton-thin AGN at X-ray energies. Here we show that this absorber is in fact both ionized and outflowing. The three phases are outflowing with velocities of the order of 1000–2000 km s<sup>−1</sup>, and there is evidence for the l-phase to be slightly faster than the other two. The c-phase ionization responds to luminosity variation on time-scales as short as a few days, demonstrating that the gas is dense enough to be in photoionization equilibrium with the continuum on short time-scales. Its clumpiness is suggested by the variation of its column density between the 2006 and the 2010 observations (as well as by the presence of a hard scattered component which contributes significantly to the X-ray spectrum in heavily absorbed data sets; see Miniutti et al. 2014). On the other hand the warm/hot phases are consistent with having the same ionization and column density on both short and long time-scales, suggesting that they are distributed in a more homogeneous way.

We show that the data are consistent with three cospatial phases with similar outflow velocities and confined between the inner (~0.1 pc) and outer (~1.6 pc) edges of the so-called clumpy, dusty torus. Moreover, under this assumption, the three phases share the same pressure. This calls for a rather natural scenario in which relatively cold, dense clouds are pressure confined by the more homogeneous warm/hot phases. Such torus-scale outflow may well represent the outer part of an outflow launched further in, which may give rise to the full system of BLR and obscuring torus in AGN replacing, with a wind solution, the classical structure of standard unification schemes (Emmering et al. 1992; Elvis 2000; Elitzur & Shlosman 2006).

The 2013 *XMM–Newton* observation is much more heavily obscured by a gas phase with one order of magnitude higher column density and ionization than in 2010. We show that this absorber is unlikely to be cospatial with the 2006 and 2010 c-phase at torus-like spatial scales, and that it must be associated with a smaller, denser structure. This places the 2013 c-phase within the dust-free BLR, although the ionization is likely too high to give rise to the observed optical broad lines.

In our analysis we detect both the BLR and the outflowing torus components, which implies that all structures are within observational reach in ESO 323–G77, possibly thanks to a particularly favourable viewing angle of ~45°, intermediate between classical Seyfert 1 and Seyfert 2 galaxies.

## ACKNOWLEDGEMENTS

This work is based on data obtained from the *Chandra* Data Archive and the *Chandra* Source Catalogue. We made use of software provided by the *Chandra* X-ray Center (CXC). We also used observations obtained with *XMM–Newton*, an ESA science mission with instruments and contributions directly funded by ESA Member States and NASA. Financial support for this work was provided by the European Union through the Seventh Framework Programme (FP7/2007–2013) under grant no. 312789. MS thanks CSIC for support through a JAE–Predoc grant, and rejects public cutbacks harmful for the common good (such as those against science). YK acknowledges support from grant DGAPA PAIIIPIT IN104215.

## REFERENCES

- Agis-González B. et al., 2014, MNRAS, 443, 2862  
 Antonucci R., 1993, ARA&A, 31, 473  
 Arnaud K. A., 1996, in Jacoby G. H., Barnes J., eds, ASP Conf. Ser. Vol. 101, Astronomical Data Analysis Software and Systems V. Astron. Soc. Pac., San Francisco, p. 17  
 Bianchi S., Piconcelli E., Chiaberge M., Bailón E. J., Matt G., Fiore F., 2009, ApJ, 695, 781  
 Blustin A. J., Page M. J., Fuerst S. V., Branduardi-Raymont G., Ashton C. E., 2005, A&A, 431, 111  
 Cash W., 1979, ApJ, 228, 939  
 Dickens R. J., Currie M. J., Lucey J. R., 1986, MNRAS, 220, 679  
 Elitzur M., Shlosman I., 2006, ApJ, 648, L101  
 Elvis M., 2000, ApJ, 545, 63  
 Elvis M., Risaliti G., Nicastro F., Miller J. M., Fiore F., Puccetti S., 2004, ApJ, 615, L25  
 Emmering R. T., Blandford R. D., Shlosman I., 1992, ApJ, 385, 460  
 Fairall A. P., 1986, MNRAS, 218, 453  
 Ferland G. J. et al., 2013, Rev. Mex. Astron. Astrofis., 49, 137  
 Gupta A., Mathur S., Krongold Y., Nicastro F., 2013, ApJ, 768, 141  
 Jiménez-Bailón E., Krongold Y., Bianchi S., Matt G., Santos-Lleó M., Piconcelli E., Scharrel N., 2008, MNRAS, 391, 1359

- Kalberla P. M. W., Burton W. B., Hartmann D., Arnal E. M., Bajaja E., Morras R., Pöppel W. G. L., 2005, *A&A*, 440, 775
- Krolik J. H., Kriss G. A., 2001, *ApJ*, 561, 684
- Krolik J. H., McKee C. F., Tarter C. B., 1981, *ApJ*, 249, 422
- Krongold Y., Nicastro F., Brickhouse N. S., Elvis M., Liedahl D. A., Mathur S., 2003, *ApJ*, 597, 832
- Longinotti A. L. et al., 2013, *ApJ*, 766, 104
- Markowitz A. G., Krumpe M., Nikutta R., 2014, *MNRAS*, 439, 1403
- Matt G., Bianchi S., Marinucci A., Guainazzi M., Iwasawa K., Jimenez Bailon E., 2013, *A&A*, 556, A91
- Miniutti G. et al., 2014, *MNRAS*, 437, 1776
- Nandra K., O'Neill P. M., George I. M., Reeves J. N., 2007, *MNRAS*, 382, 194
- Netzer H., 2008, *New Astron. Rev.*, 52, 257
- Nicastro F., Fiore F., Matt G., 1999, *ApJ*, 517, 108
- Puccetti S., Fiore F., Risaliti G., Capalbi M., Elvis M., Nicastro F., 2007, *MNRAS*, 377, 607
- Risaliti G., Elvis M., Nicastro F., 2002, *ApJ*, 571, 234
- Risaliti G. et al., 2009a, *MNRAS*, 393, L1
- Risaliti G. et al., 2009b, *ApJ*, 696, 160
- Sanfrutos M., Miniutti G., Agís-González B., Fabian A. C., Miller J. M., Panessa F., Zoghbi A., 2013, *MNRAS*, 436, 1588
- Schmid H. M., Appenzeller I., Burch U., 2003, *A&A*, 404, 505
- Smith R. K., Brickhouse N. S., Liedahl D. A., Raymond J. C., 2001, *ApJ*, 556, L91
- Torresi E., Grandi P., Longinotti A. L., Guainazzi M., Palumbo G. G. C., Tombesi F., Nucita A., 2010, *MNRAS*, 401, L10
- Véron-Cetty M. P., Véron P., 2006, *A&A*, 455, 773
- Wang J. M., Zhang E. P., 2007, *ApJ*, 660, 1072
- Zhang S. N., Ji L., Kallman T. R., Yao Y. S., Froning C. S., Gu Q. S., Kriss G. A., 2015, *MNRAS*, 447, 2671

This paper has been typeset from a  $\text{\TeX}/\text{\LaTeX}$  file prepared by the author.